Journal of Materials Chemistry A

ROYAL SOCIETY OF CHEMISTRY

PAPER

View Article Online
View Journal | View Issue

Cite this: J. Mater. Chem. A, 2022, 10, 10484

Efficient harvesting and storage of solar energy of an all-vanadium solar redox flow battery with a MoS_2@TiO_2 photoelectrode†

Gengyu Tian,[a] Rhodri Jervis,[b] Joe Briscoe,[a] Magdalena Titirici[c] and Ana Jorge Sobrido*[a]

Solar redox flow batteries constitute an emerging technology that provides a smart alternative for the capture and storage of discontinuous solar energy through the photo-generation of the discharged redox species employed in traditional redox flow batteries. Here, we show that a MoS_2-decorated TiO_2 (MoS_2@TiO_2) photoelectrode can successfully harvest light to be stored in a solar redox flow battery using vanadium ions as redox active species in both the catholyte and anolyte, and without the use of any bias. The MoS_2@TiO_2 photoelectrode achieved an average photocurrent density of ~0.4 mA cm^{-2} *versus* 0.08 mA cm^{-2} for bare TiO_2, when tested for the oxidation of V^{4+} to V^{5+}, attributed to a more efficient light harvesting and charge separation for the MoS_2@TiO_2 relative to TiO_2. The designed solar redox flow cell exhibited an optimal overall solar-to-output energy conversion efficiency (SOEE) of ~4.78%, which outperforms previously reported solar redox flow batteries. This work demonstrates the potential of the MoS_2@TiO_2 photoelectrode to efficiently convert solar energy into chemical energy in a solar redox flow battery, and it also validates the great potential of this technology to increase reliability in renewable energies.

Received 26th January 2022
Accepted 5th April 2022

DOI: 10.1039/d2ta00739h

rsc.li/materials-a

Introduction

The direct storage of sunlight in the form of hydrogen *via* overall water splitting using photoelectrochemical cells (PECs) has been the subject of extensive research in the last few decades.[1–4] The main benefit of this technology is the clean production of hydrogen through the use of solar energy.[5,6] However, the sluggish kinetics of water splitting, particularly the oxygen evolution reaction, the low overall energy conversion efficiency, and the high cost of transportation and storage of hydrogen have somewhat slowed down the take-off of the hydrogen economy.[7,8] Because of this, researchers are increasingly shifting their efforts towards the development of alternative technologies that can offer faster chemical reaction kinetics to store solar energy. Among them, solar redox flow batteries (SRFBs) have attracted recent attention. SRFBs are hybrids between PECs and redox flow batteries (RFBs). They use renewable light energy to charge redox substances and solar energy in the form of chemical energy.[9–16] One example of recent developments in this area is the SRFB designed by Yangen *et al.* that used I^{3-}/I^- and Br^-/Br^{3-} as redox active pairs.[17] The SRFB was driven by a WO_3-decorated $BiVO_4$ photoanode and provided 1.25% solar-to-output energy conversion efficiency. Yan *et al.* reported a SRFB consisting of a Li_2WO_4/LiI redox couple and a dye-sensitised TiO_2 photoelectrode, enabling a battery capacity of 0.0195 mA h mL^{-1} at a discharge density of 0.075 mA cm^{-2}.[1] Recently, Amirreza *et al.* built a tandem with a bare hematite photoanode and two dye-sensitised solar cells connected in series;[2] the conversion efficiency from solar to chemical energy of the AQDS (anthraquinone-2,7-disulfonate)/iodide SRFB using only hematite as the photoanode was about 0.1%.

Due to their high reversibility and fast reaction kinetics, all-vanadium redox flow batteries, including vanadium-based SRFBs, have been widely investigated and developed around the world.[3–6] Hao *et al.* applied a nitrogen-doped TiO_2 photoanode to a microfluidic all-vanadium photoelectrochemical cell with an average photocurrent density of 0.1 mA cm^{-2}.[7] Zi *et al.* demonstrated an AQDS/V^{4+} SRFB able to generate a relatively stable photocurrent of 0.14 mA cm^{-2} using TiO_2 nanoparticles supported on fluorine-doped tin oxide (FTO) as a photoanode.[8] Titanium dioxide (TiO_2) has been extensively investigated as a photocatalyst since the discovery of its unique properties in 1972, including remarkable stability against photocorrosion and wide band gap, large enough to provide sufficient energy to drive

[a]School of Engineering and Materials Science, Queen Mary University of London, E1 4NS, UK. E-mail: a.sobrido@qmul.ac.uk
[b]Electrochemical Innovation Lab, Department of Chemical Engineering, University College London, WC1E 7JE, UK
[c]Department of Chemical Engineering, Imperial College London, South Kensington Campus, SW7 2AZ, UK

† Electronic supplementary information (ESI) available. See https://doi.org/10.1039/d2ta00739h

a variety of useful reactions.[9–12] Although the stability of TiO_2 is excellent, the lack of visible light absorption along with the rapid recombination of photogenerated electron–hole pairs produced usually results in low quantum efficiency and poor photocatalytic activity.[13] Multiple strategies to improve the photocatalytic performance of TiO_2 have been explored, including doping with different elements,[7,14,15] decorating with noble metals,[16,17] and engineering heterojunctions with other semiconductors.[18,19] Coupling TiO_2 with other semiconductors to form heterojunctions is an effective way to boost the performance of TiO_2 (ref. 20 and 21) *via* bending of the photoelectrode band structure, which in turn provides an easier transfer path for the photogenerated electrons and holes and enables a more efficient process.[22,23] In addition, the design of a heterojunction with a semiconductor of smaller band gap provides a pathway to utilise the visible region of the solar spectrum, increasing the overall efficiency.[24,25] Some reported examples of such systems include Cu_2O@TiO_2,[26] g-C_3N_4@TiO_2 (ref. 27) and MoS_2@TiO_2.[28,29]

Here we present for the first time a SRFB with exceptional solar-to-output energy conversion efficiency (SOEE), consisting of a MoS_2@TiO_2 photoelectrode (photoanode) and carbon felt as the counter electrode (cathode). Specifically, we have studied the redox pairs V^{5+}/V^{4+} and V^{4+}/V^{3+}, whose redox potentials match the band gap of the photoelectrode heterojunction. We synthesised MoS_2@TiO_2 thin films supported on an FTO glass substrate *via* a hydrothermal route. The deposition of MoS_2 decorated TiO_2 ensured an increased specific surface area and effective light response, which translated into enhanced photon capturing and charge transfer. When sunlight reaches the photoelectrode, the photogenerated holes oxidize V^{4+} to V^{5+} at the interface between the photoelectrode and anolyte, while the photogenerated electrons reduce V^{4+} to V^{3+} at the interface between the carbon felt and catholyte. Thus, the oxidized and reduced forms of V^{4+}, V^{5+} and V^{3+}, respectively, retain the chemical energy that can be converted to electricity *via* the reverse reaction (Fig. 1). This SRFB can be written as TiO_2/MoS_2(s)|V^{4+}, V^{5+}‖V^{4+}, V^{3+}|carbon. The developed system provides a ~0.4 mA cm^{-2} photocurrent which is higher than those of similar TiO_2-based all-vanadium systems with acidic electrolytes.[7,8] This is the first time that the MoS_2@TiO_2 photoelectrode has shown good catalytic activity for vanadium redox couples, with an overall SOEE of 4.78%, remarkably higher than those of previously reported SRFB systems (Table S1, ESI†).[30,31]

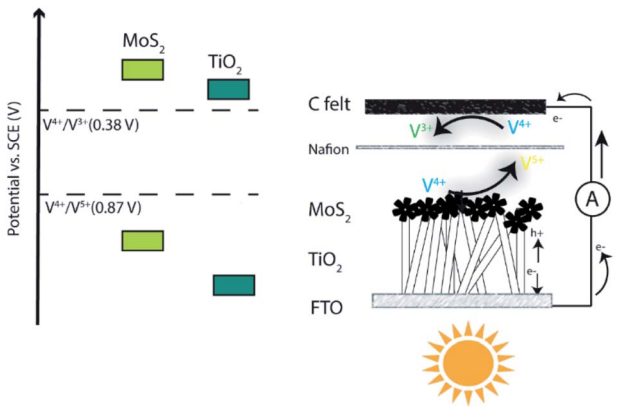

Fig. 1 Schematic representation of the SRFB system studied in this work.

Experimental

Material preparation

Preparation of TiO_2 nanorod arrays. TiO_2 nanorod arrays (NRs) on FTO were prepared using a hydrothermal method reported elsewhere.[32] Briefly, 60 mL deionised water was mixed with 30 mL of concentrated hydrochloric acid (36.5% by weight), and the solution was sonicated for 15 min. Then, 0.1, 0.3, or 0.5 mL of titanium(IV) butoxide (purum, ≥97%, gravimetric, Sigma) was added to the solution and sonicated for a further 15 min. The FTO substrates were placed into a Teflon liner (200 mL). The hydrothermal synthesis was conducted at 180 °C for 12 h. The resultant sample was rinsed extensively with deionised water, then dried at 80 °C for 1 h and thermally treated at 500 °C in air for 1 h.

Fabrication of MoS_2 nanoflowers on TiO_2 NRs (MoS_2@TiO_2). MoS_2 nanoflowers were grown on the TiO_2 NRs (0.1/0.3/0.5 mL) by a facile hydrothermal reaction.[28] Firstly, 242 mg (0.001 mol) $Na_2MoO_4 \cdot 2H_2O$ powder (99%, Sigma) and 242 mg (0.002 mol) L-cysteine (99.99%, Sigma) were mixed in 90 mL deionised water under magnetic stirring for 10 min, then transferred to a Teflon-lined autoclave and stirred for an additional 5 min. Subsequently, the TiO_2 NRs previously prepared were placed into the autoclave containing the MoS_2 precursors. The hydrothermal synthesis and deposition of MoS_2 onto the TiO_2 NRs were conducted at 200 °C for 12 h, followed by rinsing with deionized water and drying at 80 °C for 1 h. The resultant samples were labelled MoS_2@TiO_2-0.1, MoS_2@TiO_2-0.3 and MoS_2@TiO_2-0.5.

Characterisation

The morphology and microstructure of the prepared photoelectrodes were characterised using a field-emission scanning electron microscope (FESEM, Philips FEI Quanta 200 FEG) equipped with an energy dispersive X-ray spectrometer (EDS, operating at an accelerating voltage of 30 kV). The crystal phases of samples were determined by X-ray diffraction (XRD) with a Panalytical Xpert Pro diffractometer using a Cu Kα radiation source (1.5418 Å). The optical absorption properties were determined using a UV-vis spectrophotometer (Lambda 950, PerkinElmer) equipped with an integrating sphere (PerkinElmer) within a wavelength range of 350 to 800 nm and a step of 1 nm. The surface chemical states of photocatalysts were analysed by X-ray photoelectron spectroscopy (XPS, Thermo Fisher Nexsa X-ray spectrometer, Al Kα monochromatic X-ray source). ICP-MS analysis was performed using a microwave plasma atomic emission spectrometer (4210 MP-AES).

Electrochemical and photoelectrochemical characterisation

A three-electrode electrochemical cell was employed to study the electrochemical behaviour of the carbon felt electrode against vanadium ion species. The carbon felts (3.18 mm thick, 99.0%

Alfa Aesar) were pre-treated in an MTI 1200× tube furnace at 800 °C for 2 h, using a heating rate of 3 °C min^{-1} and a nitrogen flow rate of 0.5 L min^{-1}.[33] The size of the carbon felt electrodes was 1.0 cm^2 (0.32 cm^3). A KCl saturated calomel Hg_2Cl_2 electrode (SCE) and Pt foil were employed as reference and counter electrodes, respectively. Cyclic voltammetry (CV) experiments were conducted between −1.0 and 1.6 V *versus* SCE, at a scan rate of 10 mV s^{-1}, and in an electrolyte with a concentration of 0.1 M or 1.0 M V^{4+} (vanadium(IV) oxide sulfate hydrate, Sigma-Aldrich, 97%) and 1.0, 2.0 or 3.0 M H_2SO_4 (Sigma, 98%). Electrochemical impedance spectroscopy (EIS) experiments were conducted using a frequency range of 0.1 MHz to 0.1 Hz and a perturbation of 10 mV. All the electrochemical experiments were carried out using a potentiostat (Gamry IFC5000-05520).

Photoelectrochemical studies were conducted in a three-electrode electrochemical cell using TiO_2 or MoS_2@TiO_2 as a working electrode, and an SCE and Pt foil as reference and counter electrodes, respectively. 0.1 M and 1.0 M V^{4+} in 3.0 M H_2SO_4 were used as the electrolyte. Linear sweep voltammetry (LSV) measurements were conducted at a scan rate of 10 mV s^{-1} in the voltage range of −0.5 V to 0.5 V *vs.* SCE. EIS photoelectrochemical experiments were also conducted at a frequency range of 0.1 MHz to 0.1 Hz and 10 mV perturbation. The illuminated area (back illumination) of the working electrode was 1.0 cm^2. The photoelectrode was irradiated by simulated solar light (400 W Xe lamp) using an AM 1.5G filter. The power density of the incident light was calibrated to 100 mW cm^{-2} using an optical power meter with a silicon photodetector (Newport 818-SL) as a certified reference. The illuminated area of the working electrode was 1.0 cm^2.

Redox flow battery testing

Charge–discharge experiments were conducted in the voltage range 0 to 1.1 V using a current density of 1.0 mA cm^{-2} with 1.0 M V^{4+}. The electrolyte was pre-discharged to 0 V at a current density of 0.1 mA cm^{-2}. Carbon felts separated by a Nafion® membrane were used as positive and negative electrodes. The discharge current density after photocharge is 0.4 mA cm^{-2}. The carbon felts underwent the same thermal treatment described in the Electrochemical characterisation section. The Nafion membrane (115, 0.005 in. thick, DuPont de Nemours & Co) was subjected to the following treatment prior to its use: firstly, it was immersed in 50 mL 5 wt% H_2O_2 at 80 °C for 1 h, followed by treatment for an hour at 80 °C in distilled water, and another hour at 80 °C in 1.0 M H_2SO_4. The membrane was finally treated at 80 °C for 1 h in distilled water. A volume of 20 mL was employed as the initial catholyte and anolyte, respectively. The experiment was carried out using a peristaltic pump with a double head to control the flow of electrolyte on both sides of the redox flow cell to 2.5 mL min^{-1}. The size of carbon felt as the working electrode for redox flow battery testing is 5.0 cm^2 (1.59 cm^3).

Solar flow battery testing

The SRFB consisted of a modified redox flow battery (Fig. S1a, ESI†), with a window in the anolyte side to enable the irradiation of the photoanode with the Xe lamp light source, and a redox flow battery (Fig. S1b, ESI†), coupled with two electrolyte tanks and a peristaltic pump. All electrochemical data were collected using a Gamry IFC5000-05520 potentiostat. The solar flow cell assembly included the MoS_2@TiO_2 photoelectrode and carbon felt, separated by a Nafion® membrane. Both carbon felts and Nafion® membrane were pretreated as explained in the previous section. Photocharging of the SRFB was conducted without any external bias through irradiation of the photoanode using simulated solar light (400 W Xe lamp) using an AM 1.5G filter. As the SRFB photocharges, the V^{4+} present oxidises to V^{5+} in the anolyte and reduces to V^{3+} in the catholyte. EIS studies of MoS_2@TiO_2-0.5 were conducted in a SRFB configuration, using 1.0 M V^{4+} in 3.0 M H_2SO_4, frequency range 0.1 MHz–0.1 Hz and perturbation of 10 mV. The illuminated area of the working electrode in the solar flow cell was 5.0 cm^2.

Results and discussion

Three TiO_2 thin films were synthesised using different amounts of titanium(IV) butoxide (0.1, 0.3 and 0.5 mL) and deposited onto FTO using a hydrothermal route. The TiO_2 films (Fig. 2) displayed a rod-like morphology typically observed in the literature[36] with a crystal structure corresponding to rutile, as determined by X-ray diffraction (Fig. S2, ESI†).

The TiO_2 rods became larger with increasing the amount of titanium(IV) butoxide. The TiO_2 rods produced using 0.1 mL of precursor were relatively short (∼1.6 μm) and randomly oriented (Fig. 2a). As the amount of precursor is increased to 0.3 mL, generally the TiO_2 rods thickened and their length increased, by almost 1 μm, to ∼2.5 μm (Fig. 2b). However, in this case, the size, length, and orientation of the rods was still inhomogeneous. As the amount of titanium(IV) butoxide was further increased to 0.5 mL, the TiO_2 rods became much thicker (4.12 μm). Moreover, the orientation and size of the rods tended to be more uniform (Fig. 2c). The film itself also grew into a denser more compacted layer with additional titanium(IV) butoxide.

MoS_2 nanoflowers were grown on the three TiO_2 films prepared. In the case of the MoS_2@TiO_2-0.1 film, only a small amount of MoS_2 was deposited onto the TiO_2 rods, and also in the space between rods (Fig. 2d). The synthesis and growth of MoS_2 on TiO_2 with a tighter surface structure (MoS_2@TiO_2-0.3 and MoS_2@TiO_2-0.5) prevented the MoS_2 nanoflowers from depositing into the space between TiO_2 rods, leading to the formation of more uniform MoS_2 layers (Fig. 2e and f). A higher magnification of the MoS_2 nanoflowers on the upper right corner of Fig. 2f showed that each MoS_2 nanoflower had a diameter of ∼500 nm and exhibited >100 sheets. According to the literature, the higher the number of layers of MoS_2 nanosheets, the higher the photocatalytic performance, as more nanosheets will provide more active sites and area for the reaction.[32,34,35] EDS data (Fig. 2g and S3, ESI†) for the MoS_2@TiO_2-0.5 material supported the SEM data.

The UV-vis absorption spectra of TiO_2 and MoS_2@TiO_2 photoelectrodes in the front illumination mode (Fig. 3a)

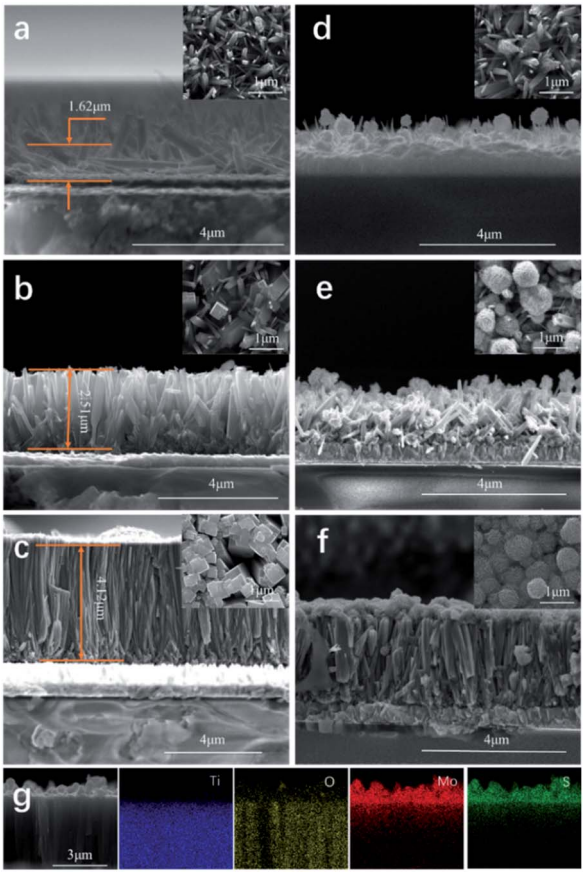

Fig. 2 SEM images of TiO_2 thin films obtained using (a) TiO_2-0.1, (b) TiO_2-0.3, (c) TiO_2-0.5, (d) MoS_2@TiO_2-0.1, (e) MoS_2@TiO_2-0.3 and (f) MoS_2@TiO_2-0.5; (g) EDS mapping of MoS_2@TiO_2-0.5.

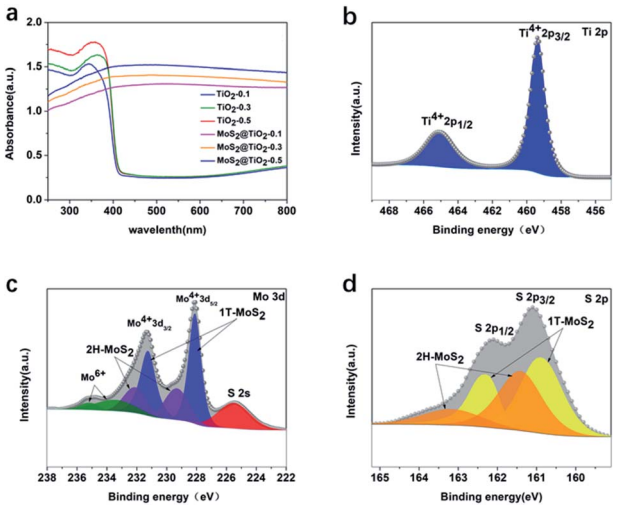

Fig. 3 UV-vis spectra of TiO_2-0.5 and MoS_2@TiO_2-0.5 using (a) front-illumination mode, XPS spectra of (b) Ti 2p from TiO_2-0.5, and XPS spectra of (c) Mo 3d and (d) S 2p from MoS_2@TiO_2-0.5.

showed an increase in light absorption within the visible range for the samples containing MoS_2, as expected. The back illumination spectra (Fig. S4, ESI†) displayed similar behaviour with additional features due to interference in the case of MoS_2@TiO_2 photoelectrodes, although some reports have suggested that the additional bands observed may be due to MoS_2.[25–30] XPS was used to analyse the oxidation state and electronic environment of Ti, Mo, S and O. The Ti 2p line XPS spectrum for TiO_2-0.5 (Fig. 3b) confirmed that the surface of TiO_2 mainly consists of Ti^{4+} $2p_{1/2}$, Ti^{4+} $2p_{3/2}$, Ti–O bond and O–H bond as expected for TiO_2, with binding energies of 465.1 eV, 459.4 eV, 530.6 eV and 532.3 eV, respectively.[32] In Fig. 3c and d, the Mo 3d and S 2p line XPS spectra for MoS_2@TiO_2-0.5 are shown, respectively. The Mo 3d line XPS spectrum indicated the existence of two different states of MoS_2: 1T-MoS_2 and 2H-MoS_2, both with Mo^{4+} as the dominant oxidation state. Previous research has indicated that the Mo 3d and S 2p XPS signals of the 1T-MoS_2 phase exhibit a higher binding energy (about 1 eV) than the corresponding signals for 2H-MoS_2.[36] The 2H and 1T phases exhibited binding energies of 229.4 and 232.2 eV for $3d_{1/2}$ and $3d_{3/2}$, respectively, for 2H-MoS_2 and 228.1 and 231.3 eV for $3d_{5/2}$ and $3d_{3/2}$, respectively, for 1T-MoS_2.[37] Two small features at 235.2 eV (Mo $3d_{3/2}$) and 233.6 eV (Mo $3d_{5/2}$) attributed to Mo^{6+} from some MoO_3 formed at the surface were also observed.[38,39] A clear peak corresponding to S 2s at 225.5 eV could also be detected. The S 2p line (Fig. 3d) exhibited two doublets corresponding to $2p_{1/2}$ and $2p_{3/2}$ at binding energies of 163.2 eV and 161.4 eV, respectively.[40] Additionally, peak contributions corresponding to bridging disulfides found in 1T-MoS_2 were observed at 162.3 eV for $2p_{1/2}$ and at 160.9 eV for $2p_{3/2}$.[41] The XPS survey spectra corresponding to TiO_2-0.5 and MoS_2@TiO_2-0.5 and the XPS O 1s line for MoS_2@TiO_2-0.5 are shown in Fig. S5, ESI.†

To study the influence of the electrolyte on the performance of the system, a CV experiment using carbon felt as a working electrode with 1.0 M/2.0 M/3.0 M sulfuric acid (without any V species) was conducted (Fig. S6, ESI†). The results showed that the ionic conductivity increased with increasing the concentration of sulfuric acid. CV and EIS of 0.1 M V^{4+} at different sulfuric acid concentrations were also conducted in a three-electrode electrochemical cell configuration (Fig. S7, ESI†). The results suggested that a higher concentration of H_2SO_4 facilitates the electrochemical reaction, resulting in more reversible redox processes at the highest concentration, 3.0 M H_2SO_4. The EIS result in Fig. S7c and d† confirmed that a higher concentration of sulfuric acid as an electrolyte can decrease the resistance through increasing the ionic conductivity of the electrolyte. The CV result indicated a redox potential difference between 0.1 M V^{3+}/V^{4+} and V^{4+}/V^{5+} of ~0.49 V in 3.0 M H_2SO_4 using thermally treated carbon felt as the working electrode (Fig. 4a). There exists a reduction peak corresponding to V^{3+}/V^{2+}; however, no peak for oxidation of V^{2+} to V^{3+} was observed. This has been previously reported in the literature, due to the extremely easy oxidation of V^{2+} in air.[42,43] In order to match the photocurrent density, 1.0 mA cm^{-2} was selected as the charge and discharge current density to test the reversibility and stability of the V^{3+}/V^{4+} and V^{4+}/V^{5+} redox pairs. The redox flow cell assembled with the same carbon felts and redox pairs exhibited a good reversibility upon charge and discharge cycling

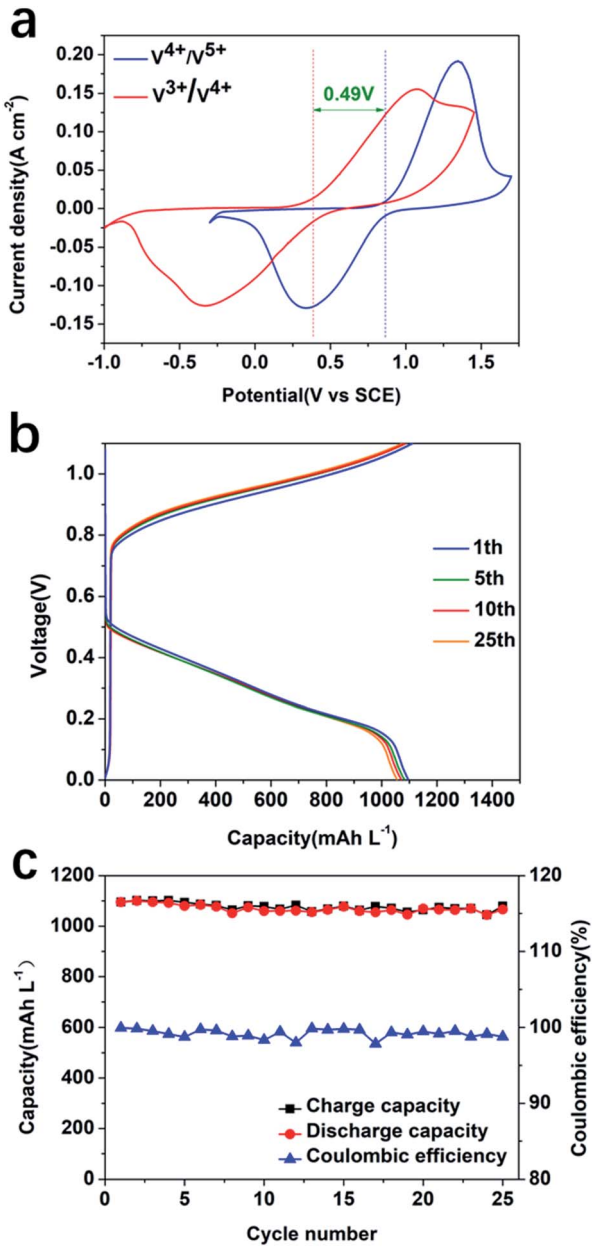

Fig. 4 (a) CV in 0.1 M V^{3+}/V^{4+} and V^{4+}/V^{5+}, with a three-electrode electrochemical cell using, in 3.0 M H_2SO_4, carbon felt, an SCE and a Pt coil as the working, reference, and counter electrodes, respectively. (b) Charge/discharge experiments for a redox flow cell using 1.0 M V^{4+}, 3.0 M H_2SO_4 electrolyte, and a current density of 1.0 mA cm^{-2} from 0 V to 1.1 V. (c) Charge–discharge capacity and coulombic efficiency of the RFB.

(Fig. 4b) with an average capacity of 1077 mA h L^{-1} and coulombic efficiency of 99.2% at a current density of 1.0 mA cm^{-2} within 25 cycles (Fig. 4c).

The redox processes of V^{4+}/V^{5+} and V^{4+}/V^{3+} redox pairs in the SRFB are summarised in eqn (1)–(3) as follows:

Anolyte:

$$V^{4+} \rightleftharpoons V^{5+} + e^- \; E_0 = 0.87 \text{ V } \textit{vs.} \text{ SCE} \quad (1)$$

Catholyte:

$$V^{3+} \rightleftharpoons V^{4+} + e^- \; E_0 = 0.38 \text{ V } \textit{vs.} \text{ SCE} \quad (2)$$

Overall:

$$2V^{4+} \rightleftharpoons V^{5+} + V^{3+} \; E_0 = 0.49 \text{ V } \textit{vs.} \text{ SCE} \quad (3)$$

After testing the performance of the RFB using V^{3+}/V^{4+} and V^{4+}/V^{5+}, the electrochemical behaviour of the TiO_2 and MoS_2@TiO_2 photoanodes against V^{4+} was examined. Fig. 5a and b show the LSV measurements in 0.1 M and 1.0 M V^{4+}, respectively, in 3.0 M H_2SO_4 for TiO_2-0.5 and MoS_2@TiO_2-0.5. The MoS_2@TiO_2 photoelectrode exhibited much higher performance than TiO_2-0.5, being able to achieve a photovoltage of ~450 mV *vs.* SCE, about 100 mV higher than that of the TiO_2-0.5 photoelectrode for both V^{4+} concentrations. Upon applying a potential bias, there is an expected increase in photocurrent for both photoelectrodes, which is also more noticeable in the case of MoS_2@TiO_2-0.5. In the case of the MoS_2@TiO_2-0.5, the increase rate is faster for the more concentrated V^{4+} electrolyte (1.0 M), reaching 0.6 mA cm^{-2} compared to ~0.4 mA cm^{-2} for 0.1 M V^{4+} at 0.4 V *vs.* SCE. Interestingly, there was no significant effect on the photocurrent response when increasing the V^{4+} concentration for the TiO_2-0.5 photoelectrode when applying a bias. We attribute this to the fact that the TiO_2 photoelectrode is already performing at its maximum capacity, in terms of the holes that can be produced at a given time, so a higher concentration of V^{4+} would not change the number of holes that can reach the electrolyte/TiO_2 interface.

Chronoamperometric measurements of all the photoelectrodes (TiO_2-0.1, TiO_2-0.3, and TiO_2-0.5 and their MoS_2@TiO_2 counterparts, Fig. S8, ESI†) conducted in a SRFB configuration showed that the performance of the samples was

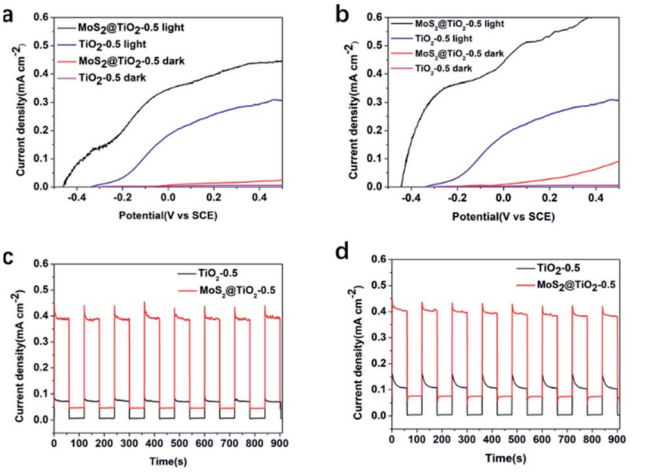

Fig. 5 LSV in (a) 0.1 M V^{4+} and (b) 1.0 M V^{4+} with a three-electrode electrochemical cell using, in 3.0 M H_2SO_4, a SCE and a Pt coil as reference and counter electrodes, respectively. Chopped-chronoamperometry experiment for a SRFB using TiO_2-0.5 or MoS_2@TiO_2-0.5 as a photoanode and thermally treated carbon felt as a cathode in (c) 0.1 M V^{4+} and (d) 1.0 M V^{4+} with 3.0 M H_2SO_4 at a 2.5 mL min^{-1} flow rate and with a light source of 100 mW cm^{-2} (AM 1.5G).

much more affected by the densification level and thickness of the TiO_2 layer than by the presence of MoS_2 in the TiO_2-0.1, TiO_2-0.3, MoS_2@TiO_2-0.1 and MoS_2@TiO_2-0.3 samples, all of which exhibited a similar photocurrent response. This is likely due to a better alignment of the TiO_2 rods for the more compact samples,[32] TiO_2-0.5 and MoS_2@TiO_2-0.5. Therefore, a significant enhancement in the photoresponse when adding MoS_2 was only observed for these more compact TiO_2 layers, with the MoS_2@TiO_2-0.5 sample exhibiting a photocurrent density of 0.4 mA cm^{-2} *versus* 0.08 mA cm^{-2} for TiO_2-0.5 in 0.1 M V^{4+}. Chopped-chronoamperometry experiments in 0.1 M (Fig. 5c) and 1.0 M V^{4+} (Fig. 5d), in 3.0 M H_2SO_4, also revealed that the MoS_2@TiO_2-0.5 photoanode presented a stable photocurrent density and quick photoresponse in V^{4+} flowing electrolyte.

A stability test was carried out for the best performing photoelectrode, MoS_2@TiO_2-0.5 in 1.0 M V^{4+}, in 3.0 M H_2SO_4 electrolyte, using a SRFB configuration. Fig. 6a shows the photocharging process conducted for five cycles. As can be observed, a full photocharge was achieved in ~60 min. As the number of charge/discharge cycles increased, the photocurrent density of MoS_2@TiO_2-0.5 decreased. After each full photocharge and discharge, the photocurrent density decreased from ~0.4 mA cm^{-2} to 0.26 mA cm^{-2} for the 5th cycle. This is attributed to the low stability of MoS_2 under the harsh acidic working conditions and more studies to protect the MoS_2 are currently being explored to mitigate this effect. The fluctuations observed in the charge profiles are due to the slow photocorrosion process affecting the MoS_2 under the acidic working environment. When the photons inject into the MoS_2@TiO_2 photoanode, the photoanode tries to create a stable equipotential interface and dynamic equilibrium between the MoS_2@TiO_2 photoanode surface and electrolyte. Due to the existence of MoS_2 photocorrosion, the interface must re-establish itself after the photocorrosion of MoS_2, leading to photocharge fluctuations. This phenomenon was also observed for the 0.1 M V^{4+} concentration electrolyte (Fig. S9a, ESI†). Fig. 6b shows the discharge experiment after each full photocharge. Compared to the poor discharge performance (25.52 mA h L^{-1} to 18.11 mA h L^{-1}) when using 0.1 M V^{4+} electrolyte (Fig. S9b, ESI†), the much higher capacity (98.93 mA h L^{-1} to 74.26 mA h L^{-1}) of 1.0 M V^{4+} (Fig. 6c) can provide higher discharge potential to overcome the multiple resistances present in the system. The coulombic efficiency for 1.0 M and 0.1 M V^{4+} after five cycles is ~90% (Fig. 7c) and ~80% (Fig. S9c, ESI†), respectively. A SOC of 9.03% after 80 min of the first photocharging cycle was observed, decreasing to 6.78% after 80 min into the fifth photocharging cycle.

During the photocharging process, the carriers from the semiconductor are excited to the conduction band and oxidise V^{4+} to V^{5+}. The photoexcitation and electron transfer can be represented as follows:

$$TiO_2 + h\nu = e^-\ (TiO_2) + h^+\ (TiO_2)\ \text{(formation) (step 1)}$$

$$e^-\ (TiO_2) + h^+\ (TiO_2) = TiO_2 + h\nu\ \text{(recombination) (step 2)}$$

$$e^-\ (TiO_2) + h^+\ (TiO_2) = e^-\ (MoS_2) + h^+\ (MoS_2)\ \text{(interface) (step 3)}$$

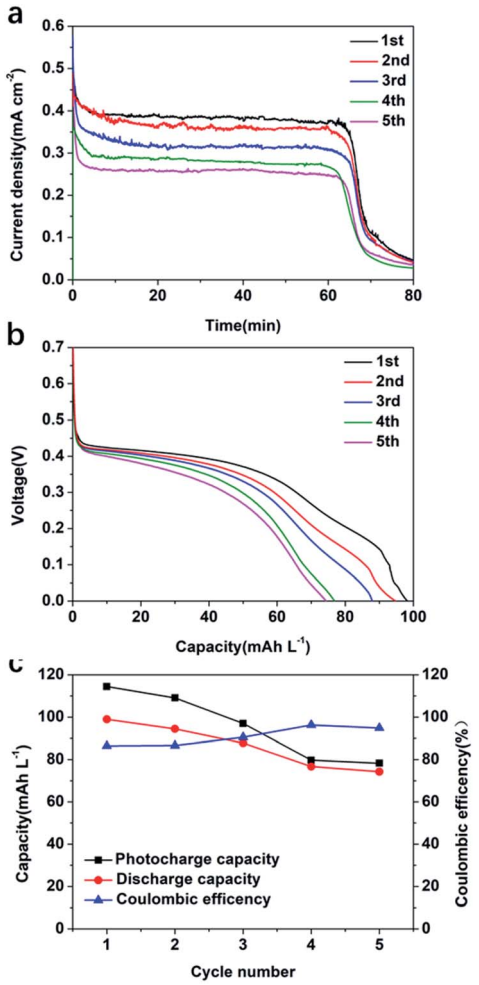

Fig. 6 (a) Cyclic photocharge and (b) discharge of MoS_2@TiO_2-0.5 and (c) the capacity and coulombic efficiency at a vanadium ion concentration of 1.0 M V^{4+}. The discharge current density is 0.4 mA cm^{-2} (100 mW cm^{-2} (AM 1.5G) with 3.0 M H_2SO_4 and a 2.5 mL min^{-1} flow rate).

$$e^-\ (MoS_2) + h^+\ (MoS_2) = MoS_2 + h\nu\ \text{(recombination) (step 4)}$$

$$V^{4+} + h^+\ (MoS_2) = V^{5+}\ \text{(production) (step 5)}$$

The average SOEE during photocharge in the SRFB was calculated according to eqn (4):[44]

$$\text{SOEE}\ (\%) = (\int I_{dis} \times dt \times \Delta E_0)/(P_{in} \times S \times t) \times 100 \quad (4)$$

where I_{dis} is the discharge current density, ΔE_0 is the potential difference of the two redox couples in the reversible state, t is the illumination time (0.5 h or 1.33 h), P_{in} is the incident solar power (100 mW cm^{-2}), and S is the area of the solar flow cell window (5.0 cm^2).

As recorded in Table 1, the calculations showed that the SOEE of the SRFB in 1.0 M V^{4+} reaches a value of 4.78% in the first cycle and remains at 3.26% in the fifth cycle.

EIS studies showed an increase in the impedance of MoS_2@TiO_2-0.5 with photocharging (Fig. S10, ESI†) reaching

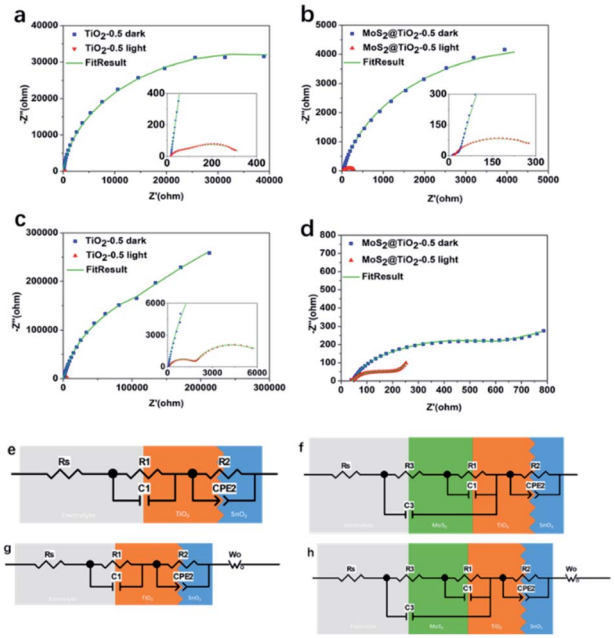

Fig. 7 EIS of TiO_2-0.5 or MoS_2@TiO_2-0.5 as the working electrode under dark and light illumination (100 mW cm^{-2}, AM 1.5G) in a three-electrode electrochemical cell using (a and b) 0.1 M V^{4+} or (c and d) 1.0 M V^{4+} in 3.0 M H_2SO_4 as an electrolyte and a KCl saturated calomel Hg_2Cl_2 electrode (SCE) and a Pt coil as the reference and counter electrodes, respectively. Equivalent circuit model used to simulate the experimental data of (e) TiO_2-0.5 and (f) MoS_2@TiO_2-0.5 in 0.1 M V^{4+} and (g) TiO_2-0.5 and (h) MoS_2@TiO_2-0.5 in 1.0 M V^{4+}.

almost three times the initial value after 2 hours, revealing an increase in resistance as the photocharging process progresses, which was attributed to the low stability of the photoelectrode under strong acid electrolyte. This was confirmed *via* SEM images acquired after each cycle (Fig. S11, ESI†). The SEM images clearly show degradation of the MoS_2 layer upon cycling and suggest that the increase in resistance observed in the EIS may be linked to this degradation of MoS_2. The photoexcitation and electron transfer may be represented as shown in eqn (S1), ESI.† The amounts of Mo and Ti leached from the photoanode were determined by ICP-MS and the results are shown in Fig. S12, ESI.† The concentration of Mo in the electrolyte increases with the number of cycles, as expected, supporting the results obtained by SEM and EIS. The TiO_2 layer was less affected by the cycling, but slight leaching was also detected for the 1.0 M V^{4+} electrolyte.

To understand the influence of the photoanode structure and to use its light absorption ability to effectively photocharge our solar flow cell, EIS was measured under both dark and light conditions for 0.1 and 1.0 M V^{4+} (Fig. 7a–d). EIS data for TiO_2 and MoS_2@TiO_2 photoanodes both for low (0.1 M V^{4+}) and high electrolyte concentration (1.0 M V^{4+}) showed that the increase in thickness of the TiO_2 leads to a decrease in impedance, an effect that remains after adding the MoS_2 layer. In the low frequency range under dark conditions, the mass transfer dominates the reaction for TiO_2-0.5.

However, under illumination, the upward trend disappears, which means that charge transfer dominates in that case (Fig. 7a and c). For MoS_2@TiO_2-0.5, EIS results demonstrate that the addition of MoS_2 to the TiO_2 layer enhances the charge transfer properties of the photoelectrode (Fig. 7b and d). Under illumination, the process remains dominated by the mass transport effect for the MoS_2@TiO_2-0.5 photoanode at low frequencies, confirming its better performance compared to TiO_2-0.5. The equivalent circuits for TiO_2-0.5 and MoS_2@TiO_2-0.5 in 0.1 M V^{4+} (Fig. 7e and f) exhibit slightly different interface components due to the differences in morphology and roughness of both photoelectrodes.[45] The EIS data taken in a three-electrode electrochemical cell and equivalent circuit for TiO_2/FTO and MoS_2@TiO_2/FTO systems show that at lower V^{4+} concentration, the diffusion resistance is also lower, because when the charge transfer dynamics are not very fast, the charge transfer process and the mass transfer process (caused by diffusion) control the overall reaction: electrochemical polarisation and concentration polarisation coexist. When the concentration is low, the charge transfer process is the rate-determining process. At higher concentration of V^{4+}, mass transport is introduced in the equivalent circuit as the Warburg impedance (W_o) in the equivalent circuit (Fig. 7g and h), in addition to the charge transfer resistance, as there is an increase in diffusion resistance with increasing concentration of V^{4+}.

The fitted data for the TiO_2-0.5 and MoS_2@TiO_2-0.5 photoelectrodes in 0.1 M V^{4+} and 1.0 M V^{4+} are consistent with the results obtained from both dark and light experiments. R_s represents the series resistance (resistance of the electrolyte solution and cable of the potentiostat), $R1$ and $C1$ represent the

Table 1 Variation of SOEE from the cycling chronoamperometry plot for the MoS_2@TiO_2 under illumination

	Sample					
	0.1 M			1.0 M		
Cycle	Photocharge capacity (mA h L^{-1})	Discharge capacity (mA h L^{-1})	SOEE (%)	Photocharge capacity (mA h L^{-1})	Discharge capacity (mA h L^{-1})	SOEE (%)
1	32.68	25.52	0.17	114.44	98.93	4.78
2	26.23	22.50	0.14	109.09	94.47	4.31
3	23.92	21.00	0.12	96.99	87.79	3.99
4	21.38	18.69	0.11	79.72	76.74	3.49
5	21.28	18.11	0.09	78.29	74.26	3.26

Table 2 Equivalent circuit main parameters of EIS

		Element						
Sample		*R*3 (Ω)	*C*3 (F)	*R*1 (Ω)	*C*1 (F)	*R*2 (Ω)	CPE2-T (F)	CPE2-P
0.1 M V^{4+}	TiO_2-0.5 dark	N/A	N/A	1.7	5.0×10^{-6}	70 441	1.9×10^{-5}	0.9
	TiO_2-0.5 light	N/A	N/A	32.9	4.3×10^{-5}	297.3	7.5×10^{-4}	0.5
	MoS_2@TiO_2-0.5 dark	6.6	3.7×10^{-6}	13.4	2.0×10^{-5}	10 160	1.9×10^{-4}	0.8
	MoS_2@TiO_2-0.5 light	3.1	1.3×10^{-5}	23.9	1.1×10^{-3}	291.3	1.4×10^{-3}	0.9
1.0 M V^{4+}	TiO_2-0.5 dark	N/A	N/A	1921	3.1×10^{-6}	2.6×10^{5}	1.4×10^{-6}	0.9
	TiO_2-0.5 light	N/A	N/A	2943	1.4×10^{-4}	1776	4.3×10^{-6}	0.8
	MoS_2@TiO_2-0.5 dark	100.2	9.3×10^{-5}	53.8	3.4×10^{-4}	377.3	5.4×10^{-4}	0.8
	MoS_2@TiO_2-0.5 light	40.5	1.1×10^{-4}	19.3	6.2×10^{-4}	30.9	2.7×10^{-3}	1.0

charge transfer resistance and capacitance of the electrolyte/TiO_2 interface in TiO_2-0.5 while in MoS_2@TiO_2-0.5 they represent the MoS_2/TiO_2 interface, and *R*2 and CPE2 represent the charge transfer equivalent structure of the interface between SnO_2 (FTO) and TiO_2. In MoS_2@TiO_2-0.5, the *R*1 and *C*1 represent the impedance of MoS_2/TiO_2. Because the MoS_2 nanoflowers cannot form a dense layer to separate the TiO_2 and the electrolyte, *R*3 and *C*3 have a collective effect representing the charge transfer resistance and capacitance of the electrolyte/MoS_2 and electrolyte/TiO_2 interfaces. The *C*3 element in parallel with *R*1, *C*1 and *R*3 is also associated with the same phenomenon. The main values of the circuit elements in the dark and in light are listed in Table 2. The results from the fitting models of TiO_2-0.1/0.3 and MoS_2@TiO_2-0.1/0.3 in 0.1 M V^{4+} and 1.0 M V^{4+} fit well with the original data in Fig. S13 and S14, ESI.† The equivalent circuit is applicable for all the TiO_2 and MoS_2@TiO_2 combinations.

Under dark conditions, due to the poor conductivity of the TiO_2, a large charge transfer resistance (R_{ct}) is generated at the interface between TiO_2 and SnO_2 (TiO_2/SnO_2), hindering electron transport. In 0.1 M V^{4+} and 1.0 M V^{4+}, under illumination, by comparing the sum of the charge transfer resistance of *R*1 + *R*2 + *R*3, it is demonstrated that the introduction of the MoS_2 interface makes it easier for electrons to transfer in the photoanode, which makes the transmission of the photogenerated electrons in the photoelectrode more efficient. In addition, the injection of photons significantly reduces the R_{ct} of the interface, especially in the TiO_2/SnO_2 interface. Due to the photon injection, many carriers are generated and moved to the interface (MoS_2/TiO_2, TiO_2/SnO_2, electrolyte/TiO_2 and electrolyte/MoS_2). The enrichment of positive and negative charges on both sides of the interface increases the capacitance under illumination. By comparing the capacitance of TiO_2 and MoS_2@TiO_2, it can be concluded that MoS_2@TiO_2 exhibits more carrier accumulation at the interface, which also confirms that the heterojunction of MoS_2@TiO_2 can effectively increase the carrier density in the photoanode.

Conclusions

TiO_2 and MoS_2@TiO_2 thin films supported on FTO were synthesised and tested as photoelectrodes in a solar redox flow battery using vanadium redox active species. Different thicknesses of the TiO_2 layer were produced. The results showed that a larger amount of Ti precursor resulted in a more uniform, thicker, and denser TiO_2 thin film with more aligned TiO_2 rods. This, in turn, led to a more efficient attachment of the MoS_2 nanoflower overlayer which also translated into a higher photocurrent response. The designed MoS_2@TiO_2 photoelectrode exhibited around 5 times higher activity than bare TiO_2 for charging the all-V SRFB tested in this work. This was attributed to a better separation of charge carriers. The SRFB with 1.0 M V^{4+} electrolyte exhibited a remarkable performance, with an average capacity of 1077 mA h L^{-1} and coulombic efficiency of 99.2% at a current density of 1.0 mA cm^{-2} within 25 cycles, charged only by solar energy without the need for any bias. The SOEE reached 4.78%. The photoelectrode interfaces were analysed in detail through EIS, and successfully confirmed the enhancement of the photocurrent response with the addition of the MoS_2 layer to the TiO_2 photoelectrode. This indicates that the highly active MoS_2@TiO_2 photoanode is promising for the enhancement of photocurrent density in the system studied. The MoS_2 facilitated charge carrier separation and provided active sites for oxidation of redox species. However, the low stability of the photoanode under strong acidic conditions led to a significant degradation of the photoelectrode after only five cycles, resulting in the leaching of metal to the electrolyte. More research is currently under way into approaches to protect the photoelectrode against degradation.

Author contributions

GT: investigation, formal analysis, methodology, visualisation, writing – original draft and editing. RJ: formal analysis, writing and editing. JB: writing and editing. MT: writing and editing. AJS: conceptualisation, formal analysis, resources, funding acquisition, writing and editing.

Conflicts of interest

There are no conflicts to declare.

Acknowledgements

The authors acknowledge Dr Ryan Wang, Jay Yan, Zhangyi Yao, Junrun Feng and Yue Wen at UCL Department of Chemical

Engineering for their help with the ICP measurements. GT acknowledges his PhD scholarship funded by the Chinese Scholarship Council. AJS acknowledges her UKRI Future Leaders Fellowship (MR/T041412/1) for funding support.

Notes and references

1 N. Yan, G. Li and X. Gao, *J. Mater. Chem. A*, 2013, **1**, 7012–7015.
2 A. Khataee, J. Azevedo, P. Dias, D. Ivanou, E. Dražević, A. Bentien and A. Mendes, *Nano Energy*, 2019, **62**, 832–843.
3 M. Skyllas-Kazacos, M. Rychcik, R. G. Robins, A. Fane and M. Green, *J. Electrochem. Soc.*, 1986, **133**, 1057.
4 M. Skyllas-Kazacos, M. Chakrabarti, S. Hajimolana, F. Mjalli and M. Saleem, *J. Electrochem. Soc.*, 2011, **158**, R55.
5 J. Vázquez-Galván, C. Flox, J. Jervis, A. Jorge, P. Shearing and J. Morante, *Carbon*, 2019, **148**, 91–104.
6 N. M. Delgado, R. Monteiro and A. Mendes, *Nano Energy*, 2021, 106372.
7 H. Feng, X. Jiao, R. Chen, X. Zhu, Q. Liao, D. Ye, B. Zhang and W. Zhang, *J. Power Sources*, 2019, **419**, 162–170.
8 Z. Wei, H. Almakrami, G. Lin, E. Agar and F. Liu, *Electrochim. Acta*, 2018, **263**, 570–575.
9 A. Fujishima, T. N. Rao and D. A. Tryk, *J. Photochem. Photobiol., C*, 2000, **1**, 1–21.
10 H. Cui, W. Zhao, C. Yang, H. Yin, T. Lin, Y. Shan, Y. Xie, H. Gu and F. Huang, *J. Mater. Chem. A*, 2014, **2**, 8612–8616.
11 T. Butburee, Y. Bai, H. Wang, H. Chen, Z. Wang, G. Liu, J. Zou, P. Khemthong, G. Q. M. Lu and L. Wang, *Adv. Mater.*, 2018, **30**, e1705666.
12 A. Fujishima and K. Honda, *nature*, 1972, **238**, 37–38.
13 K. Nakata and A. Fujishima, *J. Photochem. Photobiol., C*, 2012, **13**, 169–189.
14 U. Akpan and B. Hameed, *Appl. Catal., A*, 2010, **375**, 1–11.
15 T. Ohno, T. Mitsui and M. Matsumura, *Chem. Lett.*, 2003, **32**, 364–365.
16 V. Subramanian, E. E. Wolf and P. V. Kamat, *J. Am. Chem. Soc.*, 2004, **126**, 4943–4950.
17 Z. Zheng, B. Huang, X. Qin, X. Zhang, Y. Dai and M.-H. Whangbo, *J. Mater. Chem.*, 2011, **21**, 9079–9087.
18 C. Gao, T. Wei, Y. Zhang, X. Song, Y. Huan, H. Liu, M. Zhao, J. Yu and X. Chen, *Adv. Mater.*, 2019, **31**, e1806596.
19 M. Humayun, F. Raziq, A. Khan and W. Luo, *Green Chem. Lett. Rev.*, 2018, **11**, 86–102.
20 Y. Bessekhouad, D. Robert and J.-V. Weber, *Catal. Today*, 2005, **101**, 315–321.
21 J. Low, J. Yu, M. Jaroniec, S. Wageh and A. A. Al-Ghamdi, *Adv. Mater.*, 2017, **29**, 1601694.
22 C. Sotelo-Vazquez, R. Quesada-Cabrera, M. Ling, D. O. Scanlon, A. Kafizas, P. K. Thakur, T. L. Lee, A. Taylor, G. W. Watson and R. G. Palgrave, *Adv. Funct. Mater.*, 2017, **27**, 1605413.
23 H. Wang, L. Zhang, Z. Chen, J. Hu, S. Li, Z. Wang, J. Liu and X. Wang, *Chem. Soc. Rev.*, 2014, **43**, 5234–5244.
24 J. Li, M. Zhang, X. Li, Q. Li and J. Yang, *Appl. Catal., B*, 2017, **212**, 106–114.
25 N. Yuan, J. Zhang, S. Zhang, G. Chen, S. Meng, Y. Fan, X. Zheng and S. Chen, *J. Phys. Chem. C*, 2020, **124**, 8561–8575.
26 B. Y. Cheng, J. S. Yang, H. W. Cho and J. J. Wu, *ACS Appl. Mater. Interfaces*, 2016, **8**, 20032–20039.
27 M. Alcudia-Ramos, M. Fuentez-Torres, F. Ortiz-Chi, C. Espinosa-González, N. Hernández-Como, D. García-Zaleta, M. Kesarla, J. Torres-Torres, V. Collins-Martínez and S. Godavarthi, *Ceram. Int.*, 2020, **46**, 38–45.
28 H. He, J. Lin, W. Fu, X. Wang, H. Wang, Q. Zeng, Q. Gu, Y. Li, C. Yan and B. K. Tay, *Adv. Energy Mater.*, 2016, **6**, 1600464.
29 L. Yang, K. Majumdar, H. Liu, Y. Du, H. Wu, M. Hatzistergos, P. Y. Hung, R. Tieckelmann, W. Tsai, C. Hobbs and P. D. Ye, *Nano Lett.*, 2014, **14**, 6275–6280.
30 W. Li, H. C. Fu, L. Li, M. Caban-Acevedo, J. H. He and S. Jin, *Angew. Chem., Int. Ed. Engl.*, 2016, **55**, 13104–13108.
31 Q. Cheng, W. Fan, Y. He, P. Ma, S. Vanka, S. Fan, Z. Mi and D. Wang, *Adv. Mater.*, 2017, **29**, 1700312.
32 Y. Liu, Y. Li, F. Peng, Y. Lin, S. Yang, S. Zhang, H. Wang, Y. Cao and H. Yu, *Appl. Catal., B*, 2019, **241**, 236–245.
33 M. C. Ribadeneyra, L. Grogan, H. Au, P. Schlee, S. Herou, T. Neville, P. L. Cullen, M. D. Kok, O. Hosseinaei and S. Danielsson, *Carbon*, 2020, **157**, 847–856.
34 D. Wang, Y. Xu, F. Sun, Q. Zhang, P. Wang and X. Wang, *Appl. Surf. Sci.*, 2016, **377**, 221–227.
35 C. Liu, L. Wang, Y. Tang, S. Luo, Y. Liu, S. Zhang, Y. Zeng and Y. Xu, *Appl. Catal., B*, 2015, **164**, 1–9.
36 X. Geng, W. Sun, W. Wu, B. Chen, A. Al-Hilo, M. Benamara, H. Zhu, F. Watanabe, J. Cui and T. P. Chen, *Nat. Commun.*, 2016, **7**, 10672.
37 K. Chang, X. Hai, H. Pang, H. Zhang, L. Shi, G. Liu, H. Liu, G. Zhao, M. Li and J. Ye, *Adv. Mater.*, 2016, **28**, 10033–10041.
38 X. Zhou, M. Lickleder and P. Schmuki, *Electrochem. Commun.*, 2016, **73**, 33–37.
39 H. Liu, T. Lv, C. Zhu, X. Su and Z. Zhu, *J. Mol. Catal. A: Chem.*, 2015, **396**, 136–142.
40 H. Vrubel, D. Merki and X. Hu, *Energy Environ. Sci.*, 2012, **5**, 6136–6144.
41 M. Sun, Y. Wang, Y. Fang, S. Sun and Z. Yu, *J. Alloys Compd.*, 2016, **684**, 335–341.
42 W. Wang and X. Wang, *Electrochim. Acta*, 2007, **52**, 6755–6762.
43 M. Ulaganathan, A. Jain, V. Aravindan, S. Jayaraman, W. C. Ling, T. M. Lim, M. P. Srinivasan, Q. Yan and S. Madhavi, *J. Power Sources*, 2015, **274**, 846–850.
44 S. Liao, X. Zong, B. Seger, T. Pedersen, T. Yao, C. Ding, J. Shi, J. Chen and C. Li, *Nat. Commun.*, 2016, **7**, 11474.
45 H. Fakhr Nabavi and M. Aliofkhazraei, *Surf. Coat. Technol.*, 2019, **375**, 266–291.

